nature communications

Article

https://doi.org/10.1038/s41467-025-63319-z

Friedel oscillations and chiral superconductivity in monolayer $NbSe_2$

Received: 27 February 2025

Accepted: 14 August 2025

Julian Siegl[1], **Anton Bleibaum**[1], **Wen Wan**[2], **Marcin Kurpas**[3], **John Schliemann**[1], **Miguel M. Ugeda**[2,4,5], **Magdalena Marganska**[1,6] & **Milena Grifoni**[1]

The nature of the dominant pairing mechanism in some two-dimensional transition metal dichalcogenides is still debated. Focusing on monolayer 1H-$NbSe_2$, we show that superconductivity can be induced by the Coulomb interaction when accounting for screening effects on the trigonal lattice with multiple orbitals. Using ab initio based tight-binding parametrizations for the relevant low-energy d-bands, we evaluate the screened interaction microscopically. In the direct space, we find pronounced Friedel oscillations, a key to the Kohn-Luttinger mechanism for superconductivity. The momentum-resolved gap equations predict at the critical temperature T_c two degenerate solutions of E' symmetry, signalling the unconventional nature of the pairing. Their complex linear combination, i.e., a chiral gap with p-like symmetry, provides the ground state of the model. Our prediction of a fully gapped chiral phase well below T_c is in good agreement with the spectral function extracted from tunnelling spectroscopy measurements.

In conventional superconductors, electron pairing arises from virtual phonon exchange[1]. In this case, the slowly moving ions mediate an effective attractive interaction that allows the electrons to overcome their mutual repulsion and form Cooper pairs. This mechanism favours *s*-wave pairing, where the total spin of the electron pair is zero, and the gap function is isotropic in momentum space. Kohn and Luttinger have proposed an alternative pairing mechanism originating from pure Coulomb repulsion[2]. It is mediated by electron-hole fluctuations of the metal, which result in long-range Friedel oscillations[3] of the screened Coulomb interaction. For conventional superconductors, however, the effect is subleading compared to phonon-induced pairing[2]. When superconductivity emerges from screened repulsion, the free energy is minimised by an anisotropic gap function[4], and the pairing symmetry is associated to irreducible representations of the crystal. If the symmetry of the Bravais lattice allows a two-dimensional representation, Coulomb repulsion can even mediate a superconducting chiral phase, with spontaneous time-reversal symmetry breaking[5,6]. Two-dimensional (2D) systems with a trigonal lattice are potential candidates for becoming chiral superconductors[7–10]. Evidence for chiral superconductivity has recently been reported for tin monolayers on a Si(111) surface[11], rhombohedral multilayer graphene[12], and a transition from a nematic to a chiral phase has been proposed for TaS_2[13–15].

Pairing from repulsive interaction has been considered for a wide range of different material classes, including cuprates[16] and iron-based superconductors[17–19], heavy fermion superconductors[4], and Sr_2RuO_4[20]. More recently, these ideas have been extended to few-layer materials with flat bands[12,21] and superconducting transition metal dichalcogenide (TMD) monolayers[22–26]. The latter have attracted a lot of interest both for their potential application in novel two-dimensional electronics[27], but also their rich phenomenology, which combines strong Ising spin-orbit coupling (SOC)[28–30], superconductivity[31–33], violations of the Pauli limit in strong in-plane magnetic fields[22,34–38], and an incommensurate charge density wave[35,39,40]. The expected enhanced importance of unconventional pairing in 2D TMDs arises from their fragmented Fermi surface, cf. Fig. 1, which implies distinct

---

[1]Institute for Theoretical Physics, University of Regensburg, Regensburg, Germany. [2]Donostia International Physics Center, San Sebastián, Spain. [3]Institute of Physics, University of Silesia in Katowice, Chorzów, Poland. [4]Centro de Física de Materiales, San Sebastián, Spain. [5]Ikerbasque, Basque Foundation for Science, Bilbao, Spain. [6]Department of Theoretical Physics, Wrocław University of Science and Technology, Wrocław, Poland. e-mail: Julian.Siegl@ur.de; Milena.Grifoni@ur.de

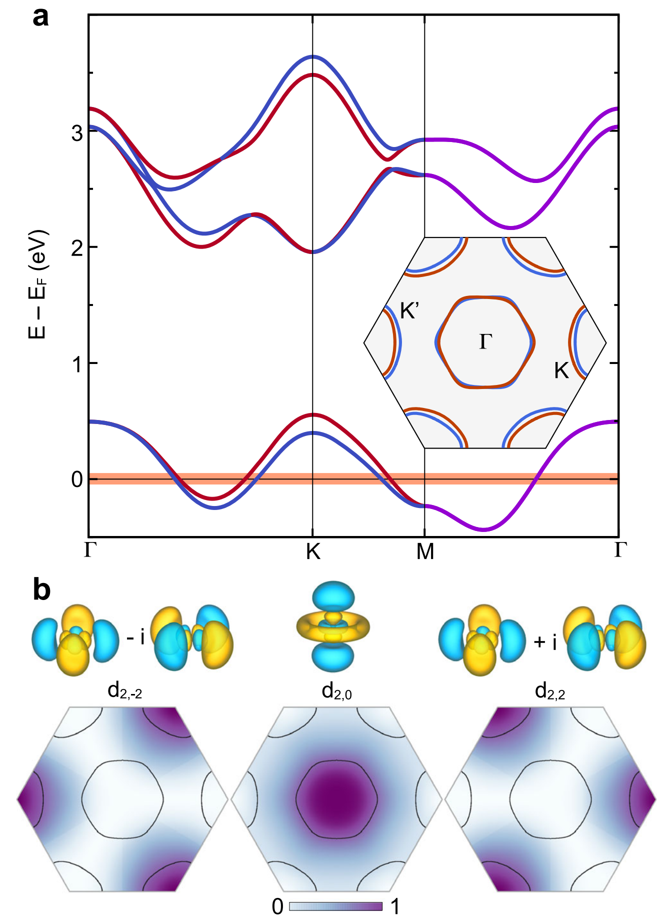

Fig. 1 | Band structure, Fermi surfaces and orbital contributions in monolayer NbSe$_2$. **a** Tight-binding Bloch bands and Fermi surfaces (inset). The Fermi energy lies within the spin-split bands crossing the Fermi level; the spin degeneracy is removed by the Ising spin-orbit coupling, resulting in spin-resolved Fermi surfaces. **b** Sketch of the three atomic $d_{l,m}$ orbitals used in the calculation and their contribution to the composition of the bands crossing the Fermi level. The quantum numbers l, m denote the total angular momentum of the orbital and its azimuthal projection.

intervalley and intravalley scattering processes, and whose amplitude can be large due to the weaker screening in lower dimensions[41,42]. Indeed, model calculations have shown that an effective attraction from competing repulsive interactions requires dominance of the short-range intervalley scattering over the long-range intravalley one[22,24,43].

In this work, we microscopically investigate the possibility of unconventional superconductivity in monolayer 1H-NbSe$_2$, a TMD whose low-energy physics is dominated by its Nb atoms. Starting from the full unscreened Coulomb interaction, we show that a generalised random phase approximation (RPA) on the trigonal lattice of Nb atoms yields a selectively screened interaction that favours short-range intervalley scattering of Cooper pairs. While bulk NbSe$_2$ is commonly assumed to be a conventional phonon-mediated superconductor[44,45], the mechanism for the monolayer limit is still actively discussed and ranges from phonon-mediated[46,47] to more exotic pairings[22,24,26,48]. Our findings, based on a microscopic calculation of the screened interaction, reinforce the possibility of unconventional superconductivity in the monolayer case. The multi-orbital character of the band crossing the Fermi level and the umklapp processes play an important role in this context. While in homogenous systems the period of Friedel oscillations in the interaction potential is provided by the Fermi wavelength[2,49], here also faster oscillations with alternating sign on neighbouring lattice sites are present. Upon solving the coupled linearised gap equations for the full screened potential, we find near T_c two degenerate p-like solutions in the E' irreducible representation of the lattice's symmetry group D_{3h}. By solving self-consistency equations, we predict the gapped $p + ip$-like chiral solution to provide the stable phase down to the lowest temperatures. The spectral function we find for this chiral gap is in very good agreement with signatures in low-temperature spectroscopy measurements.

Results

The starting point for our considerations is a tight-binding model for the Bloch band structure of monolayer NbSe$_2$ obtained by using the three most relevant orbitals of Nb, $d_{z^2} = d_{2,0}$ and $d_{2,\pm 2} = d_{x^2-y^2} \pm i d_{xy}$[50], cf. Fig. 1, fitted to ab initio calculations. Here, the parametrization by He et al.[51] is used, but similar results are obtained from the one reported by Kim & Son[52]. There are two metallic bands relevant for superconducting pairing at the Fermi level, with distinct spin, and which are split by Ising SOC[50]. As seen in the inset of Fig. 1a, multiple disjoint Fermi surfaces are present, which suggests multi-patch superconductivity similar to the one arising in the cuprates[53] and iron pnictides[16,18]. While the planar d-orbitals mostly contribute to the band composition around the K and K' valleys, $d_{2,0}$ is dominant at the Γ valley, see Fig. 1b.

In crystalline systems, the screened interaction is in general a function of both positions of the two interacting charges. It can be expanded as[41]

$$V(\mathbf{r},\mathbf{r}') = \frac{1}{\mathcal{V}} \sum_{\mathbf{q}',\mathbf{G},\mathbf{G}'} V_{\mathbf{G},\mathbf{G}'}(\mathbf{q}') e^{i(\mathbf{q}'+\mathbf{G})\cdot\mathbf{r}} e^{-i(\mathbf{q}'+\mathbf{G}')\cdot\mathbf{r}'}, \tag{1}$$

where $\mathbf{G}, \mathbf{G}'$ are reciprocal lattice vectors, $\mathbf{q}'$ is a crystal momentum not confined to lie in the plane, and $\mathcal{V}$ is the sample volume. An exact evaluation of the screened interaction is not possible. However, a closed form can be obtained in the random phase approximation (RPA), in which the polarisability is approximated by that of independent Bloch electrons[41]. With a focus on NbSe$_2$, we view the orbitals as tightly confined to the plane of the material, cf. Fig. 1. This enables us to obtain a two-dimensional version of the RPA-screened interaction, which properly accounts for the long-range behaviour. The resulting two-dimensional screened interaction $V^{\mathrm{2D,RPA}}_{\mathbf{G},\mathbf{G}'}(\mathbf{q};\omega)$ (see Supplementary Eq. (5)) can be expressed in terms of the 2D unscreened one, $V^{\mathrm{2D}}_0(\mathbf{q}) = \frac{e^2}{2\epsilon_0 q}$, as

$$V^{\mathrm{2D,RPA}}_{\mathbf{G},\mathbf{G}'}(\mathbf{q};\omega) = \epsilon^{-1}_{\mathbf{G},\mathbf{G}'}(\mathbf{q};\omega) V^{\mathrm{2D}}_0(\mathbf{q}+\mathbf{G}'), \tag{2}$$

with $\epsilon^{-1}_{\mathbf{G},\mathbf{G}'}$ the inverse of the dielectric tensor

$$\epsilon_{\mathbf{G},\mathbf{G}'}(\mathbf{q};\omega) = \delta_{\mathbf{G},\mathbf{G}'} - V^{\mathrm{2D}}_0(\mathbf{q}+\mathbf{G}) P_{\mathbf{G},\mathbf{G}'}(\mathbf{q};\omega). \tag{3}$$

The elements of the polarisability tensor in Eq. (3) are given by

$$P_{\mathbf{G},\mathbf{G}'}(\mathbf{q};\omega) = \sum_{\mathbf{p},\sigma} \chi_\sigma(\mathbf{p}+\mathbf{q},\mathbf{p};\omega) \mathcal{F}^{\sigma}_{\mathbf{p},\mathbf{p}+\mathbf{q}}(\mathbf{G}) \mathcal{F}^{\sigma *}_{\mathbf{p},\mathbf{p}+\mathbf{q}}(\mathbf{G}'), \tag{4}$$

with χ_σ accounting for electron-hole fluctuations, cf. Eq. (9), and the Bloch overlaps $\mathcal{F}$ defined as

$$\mathcal{F}^{\sigma}_{\mathbf{k},\mathbf{k}'}(\mathbf{G}) = \int_{\mathcal{V}_p} d\mathbf{r} e^{-i\mathbf{G}\cdot\mathbf{r}} \mathbf{u}^{\dagger}_{\sigma,\mathbf{k}}(\mathbf{r}) \mathbf{u}_{\sigma,\mathbf{k}'}(\mathbf{r}). \tag{5}$$

Here, $\mathbf{u}_{\sigma,\mathbf{k}}$ are Bloch spinors, i.e., the periodic part of the Bloch functions holding the information about their orbital composition, and $\mathcal{V}_p$ is the volume of the unit cell. We show in Fig. 2a the macroscopic static polarisability, the element $P_{\mathbf{0},\mathbf{0}}(\mathbf{q};\,0)$ of the polarisability tensor, properly accounting for the Bloch overlaps. In Fig. 2d the same

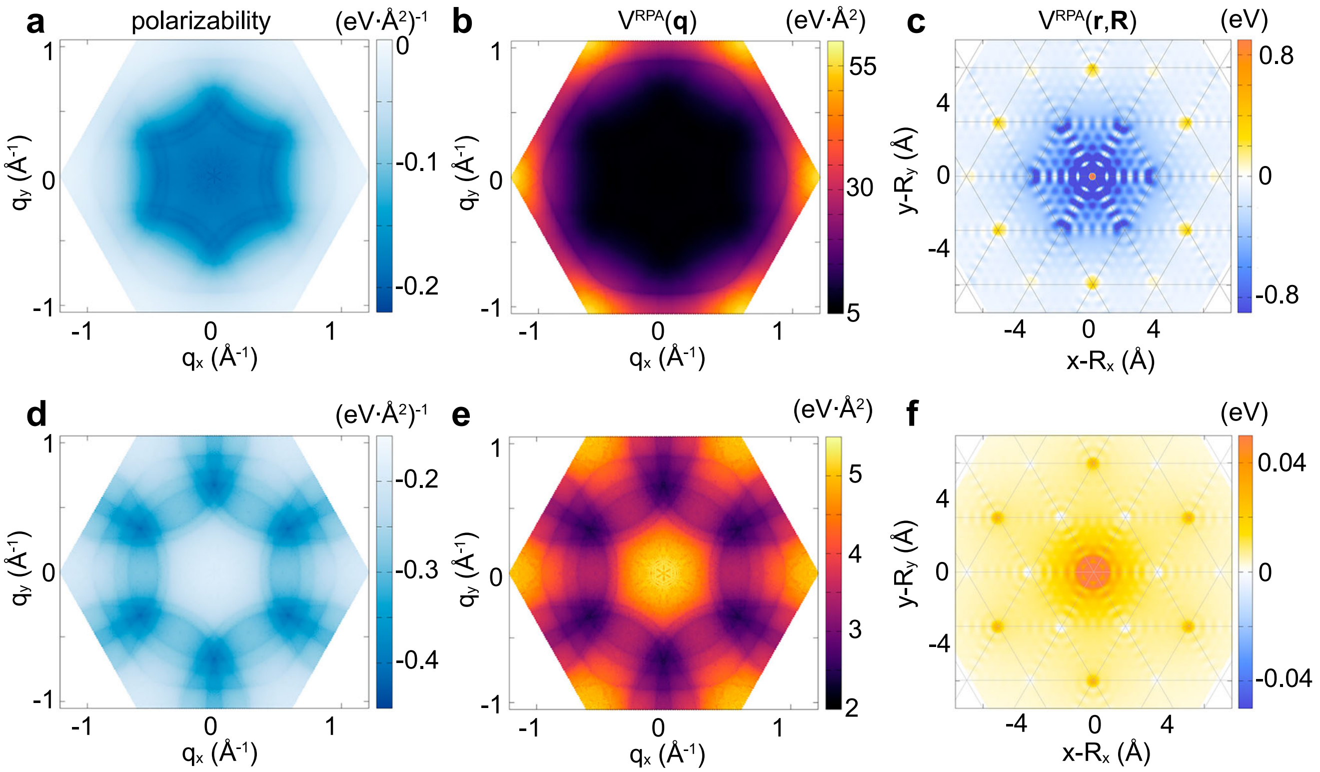

Fig. 2 | Macroscopic static polarisability and screened interaction in the reciprocal and in real space. **a** The macroscopic static polarisability $P_{\mathbf{0},\mathbf{0}}$ displays a plateau for small momentum transfers $\mathbf{q} \approx 0$ ($\mathbf{0} =: \mathbf{q}_\Gamma$), where its magnitude $|P_{\mathbf{0},\mathbf{0}}|$ attains its maximal value, and decreases for large momentum transfers $\mathbf{q} \approx \pm \boldsymbol{K}$ ($\boldsymbol{K} =: \mathbf{q}_K$). This behaviour reflects the strong momentum dependence of the Bloch overlaps. **b** The effective statically screened interaction is correspondingly strongly suppressed for small momentum transfers and exhibits maxima around $\pm \mathbf{q}_K$. **c** In real space the screened potential displays Friedel oscillations which bear signatures of the underlying trigonal lattice. The potential is strongly repulsive on-site, but attractive at the nearest-neighbour sites. **d**–**f** Same observables as in the top panels evaluated in constant-matrix-element approximation, i.e., setting the Bloch overlaps to 1. In this case, the screening at large momentum transfers is overestimated, and hence the screened interaction is largest around $\mathbf{q}_\Gamma$. In turn, the oscillations in real space are weak and the potential remains repulsive everywhere except in small regions of weak attraction.

quantity is shown in the constant-matrix-element (CME) approximation[39,52], where such overlaps are set to unity. In both cases, a plateau is observed for small momentum transfers, $\mathbf{q} \approx \mathbf{q}_\Gamma$. However, while the magnitude $|P_{\mathbf{0},\mathbf{0}}|$ of the full macroscopic polarisability is maximal there, it is minimal for the approximated one. As such, retaining the directionality of the Bloch overlaps in momentum space (see Supplementary Fig. 5) is crucial to correctly account for the long-range behaviour of the screened interaction. This qualitative difference is visualised in Fig. 2b, e, where we display the effective statically screened interaction potential $V^{\mathrm{RPA}}(\mathbf{q}) := \sum_{\mathbf{G},\mathbf{G}'} V^{\mathrm{2D,RPA}}_{\mathbf{G},\mathbf{G}'}(\mathbf{q};0)$ calculated with and without the CME approximation for the polarisability, respectively (see Methods). The effective RPA interaction potential shown in Fig. 2b is strongly suppressed for $\mathbf{q} \approx \mathbf{q}_\Gamma$, and displays maxima at $\pm \mathbf{q}_K$. The strong suppression for low momentum exchanges $\mathbf{q}$ supports the scenario of dominant intervalley scattering discussed by Hörhold et al., Roldán et al.[24,43]. In CME approximation, the effective interaction potential is, in contrast, largest at the $\mathbf{q}_\Gamma$ plateau, see Fig. 2e, while being in general smaller throughout the whole Brillouin zone. Hence, the impact of screening for large momentum electron-hole fluctuations is overestimated in the CME approximation. This is in line with earlier works that discuss the limits of the validity of this approximation for the calculation of susceptibilities in multi-orbital systems[54,55]. When turning to the real space, we find that $V^{\mathrm{RPA}}(\mathbf{r},\mathbf{r}')$, calculated according to Eq. (1), displays sizable Friedel oscillations. The interference pattern originates from the superposition of contributions from $\mathbf{q}_K$ and $-\mathbf{q}_K$ regions and is a signature of the trigonal lattice. As seen in Fig. 2c, the potential as a function of $\mathbf{r}$, with $\mathbf{r}' = \mathbf{R}$ fixed to a Nb site, exhibits an on-site repulsion at the origin and repulsive regions around the next-nearest-neighbour lattice sites, while it is strongly attractive around the nearest-neighbour sites. Figure 2f shows the real-space interaction potential in CME approximation. The screened potential there remains mostly repulsive due to weaker Friedel oscillations and displays only narrow regions of weak attraction.

The short-range part of the interaction in Fig. 2c is peaked at the origin and adjacent lattice sites. Interactions of this type are commonly approximated by the ‘top-down’ Hubbard-Kanamori model, which has previously been applied to discuss unconventional pairing in multi-orbital superconductors[18,19,55]. The Hubbard-Kanamori model has also been used for monolayer TMDs[6,7,26,51,56–59], and predicts a parameter-dependent crossover of the symmetry of the induced superconducting order[7,26]. A realistic ‘bottom-up’ calculation, either of the Hubbard-Kanamori model parameters[60] or the spatially resolved screened interaction as done here, has the advantage of enabling a determination of the interaction strength without free model parameters. These findings thus constitute a major result of the present work. As evident from Fig. 2c, and consistent with earlier works[60], the weaker screening in two dimensions results in a significant off-site and long-range contribution to the interaction in 1H-NbSe$_2$. Deriving the screened interaction first in momentum space and then obtaining its real-space representation provides a benchmark for the validity of such real-space models.

We next discuss the properties of the superconducting instability mediated by the screened potential. In general, condensates may be formed with finite center-of-mass momentum for Cooper pairs. However, the matrix elements of the screened interaction contributing to pairing are complex, with a strongly fluctuating phase resulting from

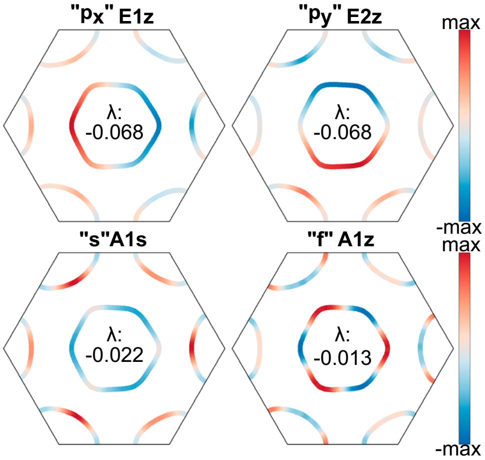

Fig. 3 | Leading instabilities as found from solving the linearised gap equations. The solutions are labeled by their approximate symmetry, the irreducible representation they belong to and whether they are majority spin singlet (*s*) or *z*-triplet (*z*). Lower eigenvalue λ indicates larger T_c of the corresponding instability. The two solutions with highest critical temperature are the two degenerate E' *z*-triplets of the D_{3h} group. The two following solutions are combinations of the A_1' *z*-triplet and singlet.

the product of Bloch overlaps, cf. Eq. (10). In absence of external magnetic fields, this tends to favour pairing between time-reversed states, whose Bloch spinors obey the relation $\mathbf{u}_{\bar{\sigma},\bar{\mathbf{k}}} = \mathbf{u}^*_{\sigma,\mathbf{k}}$, with $-\mathbf{k} = : \bar{\mathbf{k}}$, $-\sigma = : \bar{\sigma}$, resulting in a sum of real and positive contributions. We hence retain only the scattering between time-reversal partners $(\mathbf{k}, \sigma; \bar{\mathbf{k}}, \bar{\sigma})$, and consider in the following the pairing between opposite spin electrons mediated by interaction matrix elements $V_{\mathbf{k},\mathbf{k}',\sigma} : = \left\langle \mathbf{k}', \sigma; \bar{\mathbf{k}}', \bar{\sigma} | \hat{V} | \mathbf{k}, \sigma; \bar{\mathbf{k}}, \bar{\sigma} \right\rangle$ involving Kramers pairs of Bloch states. Due to Ising-SOC, the spin singlet and *z*-triplet can mix if they lie in the same irreducible representation[6]. This invalidates the typical expansion in spherical harmonics (*s*/*p*/*d*/*f*-wave), which is why we refer in the following to *s*/*p*/*d*/*f*-like gaps. A finite in-plane magnetic field would necessitate the inclusion of pairing in the *x* and *y*-triplet channels[37,56]. Restricting to time-reversal pairs yields a low-energy Hamiltonian of the BCS form[1]. Performing a mean-field approximation leads to the familiar BCS gap equation

$$\Delta_{\mathbf{k},\sigma} = -\sum_{\mathbf{k}'} V_{\mathbf{k},\mathbf{k}',\sigma} \Pi(E_{\mathbf{k}',\sigma}) \Delta_{\mathbf{k}',\sigma}, \qquad (6)$$

where the pairing function $\Pi(E) = \tanh(\beta E/2)/2E$ depends on the gap through the quasiparticle energies $E_{\mathbf{k},\sigma} = \sqrt{\xi^2_{\mathbf{k},\sigma} + |\Delta_{\mathbf{k},\sigma}|^2}$, and on the inverse temperature $\beta = 1/k_B T$. To access observables near the phase transition, we linearise Eq. (6) by replacing the excitation energies $E_{\mathbf{k},\sigma}$ in the pairing function by the single-particle energies $\xi_{\mathbf{k},\sigma}$ and solving the resulting linear problem within a range of $\pm\Lambda$ around the Fermi energy[22,26], cf. Methods.

The leading instabilities with the highest T_c are shown in Fig. 3 for the parameter set by He et al.[51] and a truncation to third nearest neighbours of the first Brillouin zone in the calculation of the matrix $V^{\mathrm{2D,RPA}}_{\mathbf{G},\mathbf{G}'}$. Due to the symmetry of the gap function under σ_h, the solutions can only belong to the irreducible representations A_1', A_2', and E' of the D_{3h} symmetry group of freestanding 1H-NbSe$_2$. We find as the dominant pairings two degenerate nematic *p*-like solutions of the E' *z*-triplet type (the singlet admixture is small), in line with the results obtained by Roy et al.[26] for their model interaction. These solutions are followed by the SOC-introduced combinations of the A_1' *s*-like singlet and *f*-like *z*-triplet that were previously discussed as candidates for the superconducting phase of monolayer NbSe$_2$[22–24,26,33], and which are the leading instabilities in multiple previous works that did not account for pairing in the E' irrep[22,56,61]. The critical temperatures of these solutions depend on the associated eigenvalues λ of the pairing matrix and the cutoff in energy. Note that a range of eigenvalues λ is reported in the literature for corresponding solutions of model Hamiltonians[22,23,26,33]. This is in line with these works using the interaction strength (and the cutoff Λ) as a fit parameter to match the critical temperature observed in experiments, e.g., $T_c \approx 2$ K in epitaxially grown samples[33] and in mechanically exfoliated ones[31]. Solving the linearised gap equation for a cutoff $\Lambda = 100$ meV, we find that the pairing strength required to yield $T_c = 2$ K is $\lambda \approx -0.154$. The difference between our result and this value is well within the uncertainty of our calculation due to the differences in the reported band structures for monolayer NbSe$_2$[26,51,52], and to the charge transfer from the substrate which was not included in our calculation (see the discussion in the Methods and Supplementary Section III B). In order to account for these uncertainties, we keep $\Lambda = 100$ meV and instead choose to rescale the resulting interaction $\hat{V} \rightarrow \gamma\hat{V}$, with $\gamma \approx 2.4$ to fix $T_c = 2$ K. Furthermore, an additional phonon-mediated interaction[1,47], e.g., by considering a momentum-independent interaction $|V_{\mathrm{ph}}| \lesssim V^{\mathrm{RPA}}(\mathbf{q}_\Gamma)$ would be sufficient to explain this discrepancy, even with unscaled $\hat{V}$. The two leading solutions of the pristine system are degenerate nematic gaps, which remain quasi-degenerate for weak enough breaking of the symmetry of the pristine system, e.g., by a substrate. This allows for the emergence of a chiral gap at temperatures below T_c[5].

The extent to which a nodal nematic solution or the gapped chiral phase is the preferred ground state in our model cannot be determined at the level of the linearised gap equation used so far. Instead, we solve the self-consistency equation, Eq. (6), as a function of temperature. Retaining the full momentum dependence in the gap equation renders the problem highly multidimensional. However, the relevant physics is captured by expanding both the interaction and the order parameter in basis functions of the appropriate irreducible representations of the crystal symmetry group[22,23,62], and solving a set of coupled equations for the expansion coefficients as a function of the temperature (see Methods). By benchmarking the pairing strength λ of the expanded solutions against the linearized calculation, this approach offers a controlled reduction of the computational cost of the calculation without significant sacrifices to the allowed momentum dependence of the order parameter. We tracked the evolution of the coefficients down to zero temperature (see Supplementary Section III A). The square root of the average square gaps (see Methods for the definition) is shown in Fig. 4a. The chiral nature of the stable solution is measured by R_{ch} and remains close to unity until very close to T_c, where any small splitting between p_x and p_y (induced here by the projection on the basis functions) results in a chiral to nematic transition. The magnitude and phase of this chiral gap at $T = 340$ mK are displayed in Fig. 4b. The free energy shown in Fig. 4c for the different candidate phases confirms that the chiral gap is physically stable within the considered temperature range (see Methods). Hence, similarly to what was possibly observed in 4Hb-TaS$_2$[14], our model predicts a chiral ground state also for monolayer NbSe$_2$.

A natural question is thus if this finding is compatible with available spectroscopic data. To this end, we turn to our own low-temperature scanning tunnelling spectroscopy (STS) measurements carried out on monolayer NbSe$_2$ on a bilayer graphene/SiC(0001) substrate (see ref. 33 for details of the setup). The measured observable is the tunnelling differential conductance (d*I*/d*V*), which is proportional to the spectral function of the sample (see Methods and Eq. (29)). The experimental d*I*/d*V* spectra recorded at different locations at 340 mK are shown in Fig. 4d and fitted to the tunnelling density of states (DOS) obtained from the chiral gap. As shown in Fig. 1, in NbSe$_2$ the quasiparticle states near the *K* and *K'* valleys arise from the planar $d_{2,\pm 2}$ orbitals, while the ones at the Γ valley have $d_{2,0}$ character and

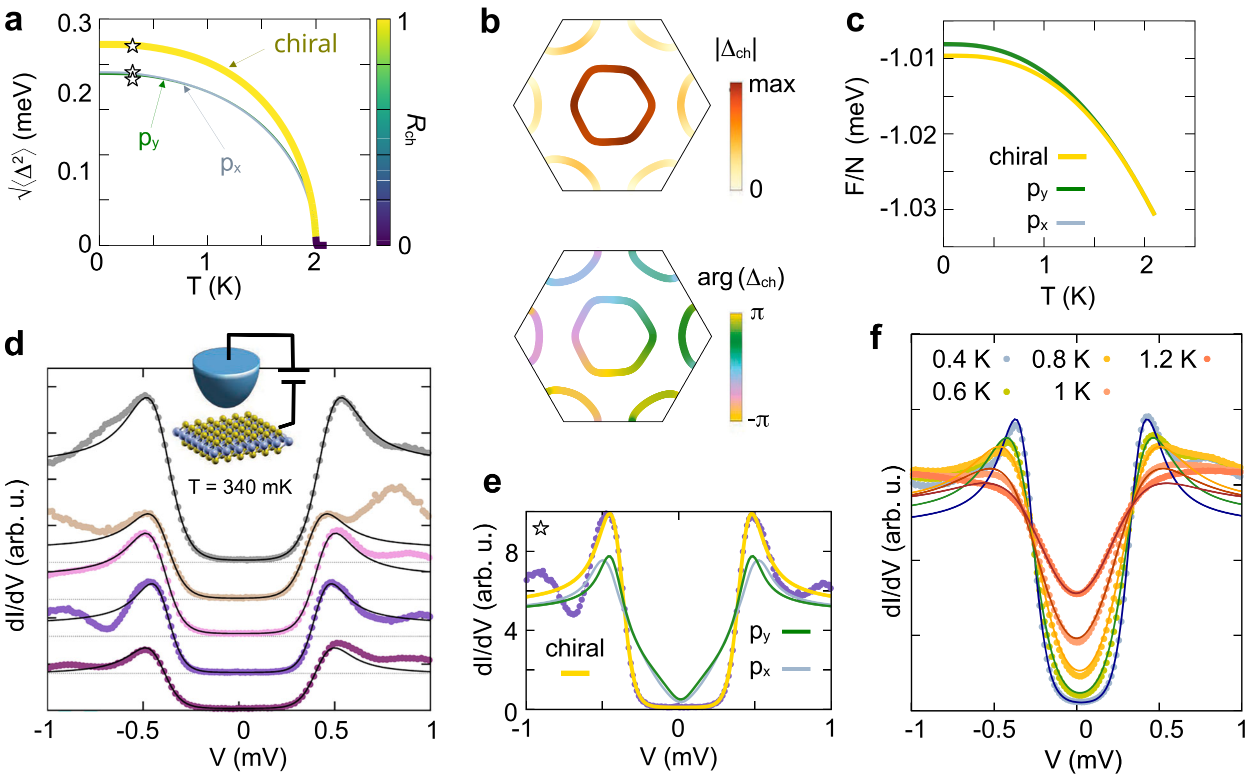

Fig. 4 | Chiral ground state and comparison with spectroscopic measurements. **a** Square root of the average square amplitude of the first three gaps solving the self-consistent gap equation as a function of temperature. The thick curve is the solution with the lowest free energy; its colour encodes the ratio R_{ch} of the contribution from a purely chiral mixture $p_x + ip_y$ of the two nematic solutions. The stars indicate the position at which the fits to the experimental curves in panel **e** were performed. **b** At $T = 340$ mK the gap equation predicts a fully gapped chiral phase of $p + ip$ type. The phase of the order parameter winds clockwise around each contiguous Fermi surface. **c** Free energy per electronic state for the first three gap solutions, calculated in the range of energies ±2 meV. The absence of nodes makes the chiral solution the favoured solution at low T. **d** Differential conductance spectra, with curves offset for clarity, recorded by STM at 340 mK, at different positions along a NbSe$_2$ monolayer grown on a bilayer graphene/SiC(0001) substrate. A clear hard gap is observed, which can be fitted using the chiral gap in (**a**). **e** One of the experimental dI/dV curves in (**d**), fitted with the gaps $\Delta_{\mathbf{k}\sigma}$ obtained from the nematic and chiral solutions of the self-consistent gap equation (see the marker in **a**). A very good agreement is found for the chiral solution on the Γ Fermi surface; the nematic ones display a clear V-shape gap that departs from the experimental data. **f** Experimental traces for different temperatures and corresponding theoretical fits with the leading Δ_{ch} shown in (**b**, **c**).

extend farther beyond the NbSe$_2$ plane. This, combined with the sensitivity of STM to states with small in-plane momentum[32,63], suggests a larger coupling to the states on the Γ Fermi surface compared to those near the K and K' valleys. The theoretical differential conductance shown in Fig. 4d is calculated using the coupling to the Γ and K Fermi pockets as free parameters (see Methods). Figure 4e shows the fit to a representative experimental dI/dV spectrum recorded at 340 mK, using both the chiral and the nematic solutions on the Γ Fermi pocket. The presence of nodal lines in the nematic phases is reflected in a V-like shape of the gap, which was not observed in the experiment. Such a shape was instead recently reported for spectroscopy experiments on monolayer 1H-TaS$_2$[64]. Finally, the temperature evolution of the differential conductance at one fixed tip location is shown in Fig. 4f. The agreement with the theoretical curves which use the temperature dependence of the gap as displayed in Fig. 4a is very good.

Discussion

While one can confidently state that the STS data are consistent with the theory presented in this work, and, in particular, with a chiral p-like E' gap at the lowest temperatures, it is clear that they alone are not conclusive evidence for this pairing symmetry. Additional insight is provided by nematic features observed in resistance experiments[38,61] under application of in-plane magnetic fields. Their presence can be explained with a transition to a nematic order parameter[38,65]. Our theory intrinsically undergoes such a transition to nematicity close to T_c if one of the in-plane symmetries of D_{3h} is broken, which can be realised, e.g., by the application of strain[65]. A fully gapped spectral function and even nematic behaviour for in-plane magnetic field are, however, also compatible with a dominant conventional s-wave pairing[33,61]. With both the Kohn-Luttinger mechanism discussed in this work and phonon-mediated pairing[47] potentially active simultaneously, the effect of their coexistence on the resulting pairing remains yet to be explored. To gather further evidence on the characterisation of the dominant mechanism, we propose testing for signatures that more strongly differentiate between the chiral p-like ground state of our theory and the s-like pairing expected from phonon-mediated pairing. Such signatures can be revealed in quasiparticle interference patterns[66], measurements of the gap at the K Fermi pockets using dynamic-STS measurements, or in the enhancement of the zero-bias conductance near the edges of superconducting domains[11].

Methods

We consider the low-energy Hamiltonian for the metallic bands of monolayer NbSe$_2$

$$\hat{H} = \sum_{\mathbf{k},\sigma} \xi_{\mathbf{k},\sigma} \hat{c}^{\dagger}_{\mathbf{k},\sigma} \hat{c}_{\mathbf{k},\sigma} + \hat{V}, \tag{7}$$

where the first term describes independent Bloch electrons in the bands crossing the Fermi level with energies $\xi_{\mathbf{k},\sigma}$, and $\hat{c}^{(\dagger)}_{\mathbf{k},\sigma}$ are the creation and annihilation operators of Bloch electrons with crystal momentum $\mathbf{k}$. The second term is the statically screened Coulomb interaction which, in the position representation $(1 \equiv \mathbf{r}, \sigma)$, is defined by a Dyson equation for its matrix elements $V(1,2) = \langle (1,2)|\hat{V}|(1,2)\rangle$ as

$$V(1,2) = V_0(1,2) + \int d(3,4) V_0(1,3) P(3,4) V(4,2), \tag{8}$$

with $V_0(1, 2)$ the matrix elements of the unscreened interaction and P the polarisability of the interacting system. We consider a trigonal 2D lattice with periodic boundary conditions composed of N prismatic unit cells of area Ω and height L with sample volume $\mathcal{V} = N\Omega L$. The derivation of Eq. (2) from Eq. (8) can be found in the Supplementary Material.

We treat the screening at the RPA level, where the full polarisability in Eq. (8) is replaced with the non-interacting polarisability tensor given by Eq. (4) where

$$\chi_\sigma(\mathbf{p}+\mathbf{q}, \mathbf{p}; \omega) = \frac{1}{N\Omega} \frac{f(\xi_{\mathbf{p}+\mathbf{q},\sigma}) - f(\xi_{\mathbf{p},\sigma})}{\omega + \xi_{\mathbf{p}+\mathbf{q},\sigma} - \xi_{\mathbf{p},\sigma} + i\eta}, \tag{9}$$

f is the Fermi function evaluated from the chemical potential μ and the overlaps $\mathcal{F}$ are defined in Eq. (5). For momenta $\mathbf{k}/\mathbf{k}'$ outside the first Brillouin zone, Eq. (5) is modified by decomposing $\mathbf{k} = \mathcal{P}(\mathbf{k}) + \mathcal{Q}(\mathbf{k})$ (see Supplementary Fig. 3), where $\mathcal{P}$ projects onto the reciprocal lattice, $\mathcal{Q}$ projects onto the associated crystal momentum and using $\mathbf{u}_{\mathbf{k},\sigma}(\mathbf{r}) = e^{i\mathcal{P}(\mathbf{k})\cdot\mathbf{r}} \mathbf{u}_{\mathcal{Q}(\mathbf{k}),\sigma}(\mathbf{r})$. We express the interaction $\hat{V}$ entering Eq. (7) in the Bloch basis. It holds for the statically screened Coulomb interaction between Bloch states (see the Supplementary Material for the full derivation),

$$\begin{aligned} &\langle \mathcal{Q}(\mathbf{k}+\mathbf{q}), \sigma; \mathcal{Q}(\mathbf{k}'-\mathbf{q}), \sigma' |\hat{V}| \mathbf{k}, \sigma; \mathbf{k}', \sigma' \rangle = \\ &\frac{1}{N\Omega} \sum_{\mathbf{G},\mathbf{G}'} V^{\text{2D, RPA}}_{\mathbf{G},\mathbf{G}'}(\mathbf{q}; 0^+) \mathcal{F}^{\sigma}_{\mathbf{k}+\mathbf{q},\mathbf{k}}(-\mathbf{G}) \mathcal{F}^{\sigma'}_{\mathbf{k}'-\mathbf{q},\mathbf{k}'}(\mathbf{G}'), \end{aligned} \tag{10}$$

where $\mathbf{k}, \mathbf{k}'$ and $\mathbf{q}$ are in-plane momenta restricted to the first Brillouin zone. Noting that the dominant contribution to the matrix element is due to the first few nearest-neighbour sites (see Supplementary Section II D for a discussion) we introduce an effective interaction potential

$$\begin{aligned} &\langle \mathcal{Q}(\mathbf{k}+\mathbf{q}), \sigma; \mathcal{Q}(\mathbf{k}'-\mathbf{q}), \sigma' |\hat{V}| \mathbf{k}, \sigma; \mathbf{k}', \sigma' \rangle = \\ &\approx \frac{1}{N\Omega} \left(\sum_{\mathbf{G},\mathbf{G}'} V^{\text{2D, RPA}}_{\mathbf{G},\mathbf{G}'}(\mathbf{q}) \right) \mathcal{F}^{\sigma}_{\mathbf{k}+\mathbf{q},\mathbf{k}}(\mathbf{0}) \mathcal{F}^{\sigma'}_{\mathbf{k}'-\mathbf{q},\mathbf{k}'}(\mathbf{0}') \\ &=: \frac{1}{N\Omega} V^{\text{RPA}}(\mathbf{q}) \mathcal{F}^{\sigma}_{\mathbf{k}+\mathbf{q},\mathbf{k}}(\mathbf{0}) \mathcal{F}^{\sigma'}_{\mathbf{k}'-\mathbf{q},\mathbf{k}'}(\mathbf{0}'), \end{aligned} \tag{11}$$

where we restrict $\mathbf{G}, \mathbf{G}'$ to the range where $\mathcal{F}(\mathbf{G}) \approx \mathcal{F}(\mathbf{0})$ holds, i.e., up to third nearest neighbouring Brillouin zones. This effective interaction potential enables a discussion of the screened interaction on the lattice in terms of a simple $\mathbf{q}$-dependent quantity shown in Fig. 2, but is not used for the calculation of the pairing, where we keep the dependence of the Bloch factors $\mathcal{F}$ on $\mathbf{G}$.

To access the possible superconducting instabilities described by Eq. (6), we solve a linearised form of the gap equation. First, we project the gap equations on the Fermi surfaces by introducing a local density of states $\rho_{\mathbf{k},\sigma}$ along the Fermi surfaces. We restrict the allowed momenta $\mathbf{k}'$ in Eq. (6) to a range around the Fermi surfaces given by a cutoff $\pm\Lambda$ in energy. Next, we convert the sum over the transverse component $\mathbf{k}' - \mathbf{k}_\text{F}$ into an integral in energy over this range $[-\Lambda, \Lambda]$. Assuming that the gap and the interaction vary slowly in this thin shell around each Fermi surface, we can approximate $\Delta_{\mathbf{k}',\sigma} \approx \Delta_{\mathbf{k}_\text{F},\sigma}$ and $V_{\mathbf{k},\mathbf{k}',\sigma} \approx V_{\mathbf{k},\mathbf{k}_\text{F},\sigma}$. The resulting gap equation with $\mathbf{k}, \mathbf{k}'$ on the Fermi surfaces takes the form

$$\Delta_{\mathbf{k},\sigma} = -\sum_{\mathbf{k}' \in \text{FS}} V_{\mathbf{k},\mathbf{k}',\sigma} \int_{-\Lambda}^{\Lambda} d\xi \rho_{\mathbf{k}',\sigma}(\xi) \Pi(E_{\mathbf{k}'\sigma}) \Delta_{\mathbf{k}',\sigma}, \tag{12}$$

with the pairing function $\Pi(E) = \tanh(\beta E/2)/2E$. Close to T_c we have $\Pi(E) \approx \Pi(\xi)$ and Eq. (12) becomes a set of linear equations. Instead of starting from the statically screened interaction and applying the mean-field approximation, an alternative approach to the problem is provided by investigating the pair-scattering vertex where the problem also simplifies to the real and static part of the effective pairing interaction[18,55]. The problem of finding the shape of the order parameter along the Fermi surfaces is equivalent to determining the kernel of a matrix $\mathbb{M}_\sigma$, whose indices are the momenta $\mathbf{k}_\text{F}$ on the Fermi surface, as

$$\mathbb{M}_\sigma \boldsymbol{\Delta}_\sigma = 0, \tag{13}$$

where, $\forall \mathbf{k}, \mathbf{k}' \in \text{FS}$,

$$(\mathbb{M}_\sigma)_{\mathbf{k},\mathbf{k}'} = \delta_{\mathbf{k},\mathbf{k}'} + V_{\mathbf{k},\mathbf{k}',\sigma} \rho_{\mathbf{k}',\sigma} \alpha^0(T, \Lambda), \tag{14}$$

$$\alpha^0(T, \Lambda) = \int_0^\Lambda d\xi \frac{\tanh(\beta\xi/2)}{\xi}. \tag{15}$$

Here, we assumed a flat density of states $\rho_{\mathbf{k},\uparrow}(\xi) \approx \rho_{\mathbf{k},\uparrow}$ within the energy range $\pm\Lambda$ around the chemical potential. We rewrite $\mathbb{M}_\sigma$ by factoring out the energy integral α^0 in the second summand as

$$\mathbb{M}_\sigma = \mathbb{1} + \alpha^0(T, \Lambda) \mathbb{U}_\sigma, \tag{16}$$

where $\mathbb{U}_\sigma$ is the pairing matrix containing the interaction and local density of states along the Fermi surfaces. The possible superconducting pairings solving Eq. (13) are the eigenvectors of $\mathbb{U}_\uparrow$ with the corresponding eigenvalues λ_i fulfilling

$$\lambda_i = -1/\alpha^0(T_{\text{c},i}, \Lambda), \tag{17}$$

and $T_{\text{c},i}$ the critical temperature of the respective instability. The cutoff Λ sets an energy scale against which to measure the gaps and T_c, similar to the Debye frequency in the usual BCS-theory[1]. In general, not all eigenvectors of $\mathbb{U}_\sigma$ found in this way correspond to physically stable situations[67]. Similarly, the requirement of vanishing $\Delta_{\mathbf{k},\sigma}$ close to $T_{\text{c},i}$ is only fulfilled if no other superconducting phase with higher T_c is present. As such, we expect only the solution with the highest T_c to be realised. Due to the monotonic nature of $\alpha^0(T, \Lambda)$ as a function of both T and Λ, the solution with the highest critical temperature always corresponds to the lowest negative eigenvalue λ of the pairing matrix. As Λ is a model parameter, we classify and discuss the strength of the different instabilities by their eigenvalues λ_i.

To investigate how the gaps evolve at temperatures below T_c, we solve Eq. (12) without linearizing. Since we want to use the approximations $\Delta_{\mathbf{k}',\sigma} \approx \Delta_{\mathbf{k}_\text{F},\sigma}$ and $V_{\mathbf{k},\mathbf{k}',\sigma} \approx V_{\mathbf{k},\mathbf{k}_\text{F},\sigma}$, we fix the cutoff to the value of Λ = 0.1 eV which, together with the rescaling of the screened interaction to $\hat{V}_\gamma := \gamma\hat{V}$ as discussed in the main text, yields T_c = 2 K. This enables us to fit to the experimental T_c while retaining the shape of the interaction as found from our calculation of the screened Coulomb interaction. Since the macroscopic polarisability $P_{\mathbf{0},\mathbf{0}}$ calculated from DFT (see Supplementary Section I B) is even lower at intermediate momentum transfers than our results from a tight-binding calculation, it is plausible that the screened interaction in absence of the substrate is even stronger than our $\hat{V}$. This is to be expected, since the inclusion of the Se p-orbitals, which contribute most noticeably near the M points, would further diminish the overlaps between states on the Fermi surface, resulting in lower screening.

We expand the gap for one spin species in terms of a restricted set of basis functions, corresponding to the irreducible representations of the symmetry group D_{3h}, as

$$\forall_{\mathbf{k}\in\pi}: \quad \Delta_{\mathbf{k},\uparrow} = \sum_{\mu} f_{\mu}^{\pi}(\mathbf{k})\Delta_{\mu}^{\pi}, \tag{18}$$

where μ labels basis functions and $\pi \in \{\Gamma, K\}$ the Fermi surfaces[22,43]. We orthonormalise our basis functions with respect to the number N_π of momenta on each Fermi surface π to satisfy

$$\left\langle f_{\mu}^{\pi}, f_{\mu'}^{\pi}\right\rangle_{\pi} := \frac{1}{N_\pi}\sum_{\mathbf{k}\in\pi} f_{\mu'}^{\pi}(\mathbf{k}) f_{\mu}^{\pi}(\mathbf{k}) = \delta_{\mu,\mu'}. \tag{19}$$

Using this orthogonality, we reduce the dimensionality of the self-consistency problem drastically by projecting the gap equation into a form that couples only the expansion coefficients Δ_{μ}^{π}[22]. It reads

$$\Delta_{\mu}^{\pi} = -\frac{1}{N_\pi}\sum_{\pi',\mu'}\sum_{\substack{\mathbf{k}\in\pi \\ \mathbf{k}'\in\pi'}} f_{\mu}^{\pi}(\mathbf{k}) V_{\mathbf{k},\mathbf{k}',\uparrow}\rho_{\mathbf{k}',\uparrow}\alpha_{\mathbf{k}'}^{\pi'} f_{\mu'}^{\pi'}(\mathbf{k}')\Delta_{\mu'}^{\pi'}, \tag{20}$$

where the pairing strength $\alpha_{\mathbf{k}}^{\pi}$ is given by

$$\alpha_{\mathbf{k}}^{\pi} = \int_0^{\Lambda} d\xi\, \frac{\tanh(\beta E(\xi, \Delta_{\mathbf{k}}^{\pi})/2)}{E(\xi, \Delta_{\mathbf{k}}^{\pi})}. \tag{21}$$

At T_c, the pairing strength $\alpha_{\mathbf{k}}^{\pi}$ becomes independent of $\mathbf{k}$ and π. In this case, the orthogonality Eq. (19) yields a linearised gap equation for the expansion coefficients

$$\Delta_{\mu}^{\pi} = -\alpha^0 \sum_{\pi',\mu'} U_{\mu,\mu'}^{\pi,\pi'}\Delta_{\mu}^{\pi'}, \tag{22}$$

where the pairing matrix $\mathbb{U}$ in this representation is given by

$$U_{\mu,\mu'}^{\pi,\pi'} = \frac{1}{N_\pi}\sum_{\mathbf{k}\in\pi,\mathbf{k}'\in\pi'} f_{\mu}^{\pi}(\mathbf{k}) V_{\mathbf{k},\mathbf{k}',\uparrow}\rho_{\mathbf{k}',\uparrow} f_{\mu'}^{\pi'}(\mathbf{k}'). \tag{23}$$

To account for the mixing between different symmetries due to the $\mathbf{k}$ dependence of $\alpha_{\mathbf{k}}^{\pi}$ below T_c, we insert a unity in Eq. (20) to arrive at

$$\Delta_{\mu}^{\pi} = -\sum_{\pi',\mu',\mu''} U_{\mu,\mu'}^{\pi,\pi'}\Upsilon_{\mu',\mu''}^{\pi'}\Delta_{\mu''}^{\pi'}, \tag{24}$$

where the mixing of different basis functions is described by

$$\Upsilon_{\mu,\mu'}^{\pi} = \frac{1}{N_\pi}\sum_{\mathbf{k}\in\pi} f_{\mu}^{\pi}(\mathbf{k})\alpha_{\mathbf{k}}^{\pi} f_{\mu'}^{\pi}(\mathbf{k}). \tag{25}$$

For an incomplete set of basis functions this insertion of unity becomes approximate, but in our case still suffices to capture the weak mixing between basis functions induced by $\alpha_{\mathbf{k}}^{\pi}$. As such, we employ Eq. (24) to numerically determine the evolution of the solutions obtained from the linearised equations below their $T_{c,i}$. The basis functions we used and the temperature dependence curves for the respective expansion coefficients are shown in Supplementary Section III A.

We define a purely chiral solution as

$$\Delta_{\mathrm{p+ip}} = \frac{||\Delta_{\mathrm{py}}||}{||\Delta_{\mathrm{px}}||}\Delta_{\mathrm{px}} + i\Delta_{\mathrm{py}}, \tag{26}$$

where $||\Delta|| := \sqrt{\sum_{\pi=G,K}\langle\Delta,\Delta\rangle_\pi}$, with the scalar product defined in Eq. (19). The Δ_{px} component is renormalised so that both nematic solutions enter with the same weight. The ratio of admixture R_{ch} of $\Delta_{\mathrm{p+ip}}$ in the chiral solution Δ_{ch} in Fig. 4a is defined as

$$R_{\mathrm{ch}} := \frac{|\sum_{\pi=\Gamma,K}\langle\Delta_{\mathrm{p+ip}},\Delta_{\mathrm{ch}}\rangle_\pi|}{||\Delta_{\mathrm{ch}}||\,||\Delta_{\mathrm{p+ip}}||}. \tag{27}$$

The square root of mean squared Δ shown in Fig. 4a for each gap symmetry is $\sqrt{\langle\Delta^2\rangle} \equiv ||\Delta||$.

The free energy of a superconductor with gap $\Delta_{\mathbf{k}\sigma}$ can be written as

$$\begin{aligned} F = {} & \frac{1}{2}\sum_{\mathbf{k}\sigma}\left(\xi_{\mathbf{k}\sigma} - E_{\mathbf{k}\sigma} + \Pi(E_{\mathbf{k}\sigma})|\Delta_{\mathbf{k}\sigma}|^2\right) \\ & - k_{TB}T\sum_{\mathbf{k}\sigma}\ln\left(1 + e^{-E_{\mathbf{k}\sigma}/k_{TB}T}\right). \end{aligned} \tag{28}$$

Note that this free energy is written assuming that the gap obeys the self-consistent equations (see Supplementary Section III). It cannot be used to find the physical gaps by minimization with respect to $\Delta_{\mathbf{k}\sigma}$, but does yield the correct result once a solution is found by solving the self-consistent gap equations[67]. We therefore use it to rank the solutions by their free energy gain within the energy window of ± 2 meV where the contributions of different gap symmetries are distinguishable.

NbSe$_2$ monolayers$_2$ were grown on graphitised (bilayer graphene) on 6H-SiC(0001) by molecular beam epitaxy (MBE) at a base pressure of $\sim 2\cdot 10^{-10}$ mbar in our home-made ultrahigh-vacuum (UHV) MBE system. SiC wafers with resistivities $\rho \sim 120\,\Omega$cm were used[68].

Reflective high-energy electron diffraction (RHEED) was used to monitor the growth of the NbSe layer$_2$. During the growth, the bilayer graphene/SiC substrate was kept at 580 °C. High-purity Nb (99.99%) and Se (99.999%) were evaporated using an electron beam evaporator and a standard Knudsen cell, respectively. The Nb:Se flux ratio was kept at 1:30, while evaporating Se led to a pressure of $\sim 5\cdot 10^{-9}$ mbar (Se atmosphere). Samples were prepared using an evaporation time of 30 min to obtain a coverage of ~ 1 ML. To minimise the presence of atomic defects, the evaporation of Se was subsequently kept for an additional 5 minutes. Atomic force microscopy (AFM) under ambient conditions was routinely used to optimise the morphology of the NbSe$_2$ layers. The samples used for AFM characterization were not further used for the scanning tunnelling microscope (STM). Lastly, to transfer the samples from our UHV-MBE chamber to our STM, they were capped with a ~10 nm amorphous film of Se, which was subsequently removed by annealing at the STM under UHV conditions at 280 °C.

Scanning tunnelling microscopy/spectroscopy experiments were carried out in a commercial low-temperature, high magnetic field (11 T) UHV-STM from Unisoku (model USM1300) operated at T = 0.34 K unless otherwise stated. STS measurements (using Pt/Ir tips) were performed using the lock-in technique with typical ac modulations of 20–40 μV at 833 Hz. All data were analyzed and rendered using WSxM software[69]. To avoid tip artifacts in our STS measurements, the STM tips used for our experiments were previously calibrated on a Cu(111) surface. A tip was considered calibrated only when tunnelling spectroscopy performed on Cu(111) showed a sharp surface state onset at −0.44 eV followed by a clean and monotonic decay of the differential conductance signal (i.e., dI/dV). In addition to this, we also inspected the differential conductance within ±10 mV to avoid strong variations around the Fermi energy.

Table 1 | Fit coefficients for comparison between STS experiment and theory in Fig. 4(e)

Solution	C_K, C_Γ [nS eV Å^2]	A	V_0 [mV]	G_0 [nS]	T_{eff}/T
ch	3.84 E-6, 8.20	1.17	1.26 E-2	5.89 E-3	1.31
p_x	0.00 E-9, 7.93	1.08	1.22 E-2	0.00 E-9	1.01
p_y	0.00 E-9, 7.90	1.17	1.29 E-2	0.00 E-9	1.01

The best fit for each solution is achieved by selective coupling to the Γ pocket in line with the arguments presented above. The coupling to the K pockets is too small to reliably be determined by the fitting routine in presence of both broadening and noise.

For spectroscopy in the tunnelling regime with a normal metal tip, the differential conductance is given by

$$G(V) = \sum_{\mathbf{k},\sigma} C_{\mathbf{k}\sigma} \int_{-\infty}^{\infty} \frac{\mathrm{d}E}{2\pi} A_\mathrm{s}(\mathbf{k},\sigma;E)\left(-\frac{\partial f(E+eV)}{\partial E}\right), \tag{29}$$

where A_s is the spectral function of the superconductor. The coupling $C_{\mathbf{k}\sigma}$ accounts for the spectral function of the tip and the tunnelling overlap between the tip's evanescent states and quasiparticle states from the superconductor with momentum $\mathbf{k}$ and spin σ. We do not expect the coupling to vary much on any given Fermi surface π, and as such we approximate $C_{\mathbf{k},\sigma} \approx C_\pi$. However, due to the different orbital composition and in-plane momenta of the quasiparticle states at the K, K' valleys and at the Γ surface, cf. Fig. 1b, the coupling constant will be in general different. In particular, since the $d_{2,0}$ orbital extends farthest out of plane and the STM favours states with small in-plane momentum[63], as has been observed in previous STM measurements[32], we expect $C_\Gamma \gg C_K$.

In the tunnelling regime, where the experimental data was taken, the lifetime of the quasiparticles is weakly affected by the coupling to the tip and the spectral function can be approximated with the local density of states of the quasiparticles, $A_\mathrm{s}(\mathbf{k}, \sigma, E) = 2\pi D_{\mathbf{k},\sigma}(E)$. The tunnelling to each of the Fermi surfaces represents a distinct transport channel, whose strength is given by the sum over the local density of states

$$D_{\pi,\sigma}(E) = \sum_{\mathbf{k}\in\pi} D_{\mathbf{k},\sigma}(E). \tag{30}$$

The latter are modeled by assuming a BCS form factor modifying the local density of states $\rho_{\mathbf{k},\sigma}$ in the normal conducting state as

$$D_{\mathbf{k},\sigma}(E) = \rho_{\mathbf{k},\sigma}\mathrm{Re}\sqrt{\frac{E^2}{E^2 - |\Delta_{\mathbf{k},\sigma}|^2}}. \tag{31}$$

In the absence of magnetic fields, we can assume that, due to time reversal symmetry, $D_{\pi,\sigma} = D_\pi/2$ and $C_{\pi,\sigma} = C_\pi$. As such, Eq. (29) predicts for the total differential conductance a superposition of contributions from the distinct transport channels with weights provided by the couplings C_π as

$$G(V) \approx \sum_\pi C_\pi G_\pi(V), \tag{32}$$

$$G_\pi(V) = \int_{-\infty}^{\infty} \mathrm{d}E\, D_\pi(E)\left(-\frac{\partial f(E+eV)}{\partial E}\right). \tag{33}$$

For low temperature, the form of the gap on each separate Fermi surface results in characteristic signatures in the differential conductance of the respective transport channel. We use as a fit function this superposition of the differential conductance of the individual transport channels. For the gaps on the Fermi surfaces $\Delta_{\mathbf{k},\sigma}$, we use the form of the gaps as found from Eq. (24) at the experimental temperature T_exp indicated by stars in Fig. 4a. For single-band s-wave superconductors the ratio between the amplitude of the gap and the critical temperature is fixed as $\Delta(T = 0\,\mathrm{K})/(k_\mathrm{B}T_\mathrm{c}) = \pi e^{-\gamma_\mathrm{e}} \approx 1.76$, with Euler's constant γ_e[1]. This ratio appears to be slightly violated in monolayer 1H-NbSe$_2$ as the expected s-wave gap for the $T_\mathrm{c} \approx 2\,\mathrm{K}$ is $\Delta(T = 0\,\mathrm{K}) \approx 0.3$ meV instead of the roughly 0.4−0.5 meV gap we find in the spectral function, in agreement with earlier works[33]. Such violations of the BCS-ratio are known to occur in multi-band or multi-patch superconductors and have been observed previously[18,70]. To account for this possibility, we allow for a fit of the amplitude of our solution by a common rescaling of all $\Delta_{\mathbf{k},\sigma}$ by a parameter A as $\Delta_{\mathbf{k},\sigma} \to A\Delta_{\mathbf{k},\sigma}$. The latter also takes care of the uncertainty of the actual experimentally realised T_c and the rescaling factor γ of the interaction.

To qualitatively account for additional sources of broadening in the experiment, we fit with an effective temperature T_eff in the calculation of the derivative in Eq. (33) which ranges between 1.3 and 1.4 times the recorded base temperature of the STM in Fig. 4d, e and is kept at 1.4 times the measurement temperature for Fig. 4f. To account for offsets in the calibration, we further allow for both a small constant offset G_0 in the measured conductivity and V_0 in the recorded voltage. The fit coefficients for the other traces shown in Fig. 4d, f only differ by small quantitative changes from the ones reported in Table 1 for Fig. 4e. For the fitting we use the trust region reflective algorithm as implemented in SciPy's "curve_fit" routine. We consider a range of ± 0.5 mV containing the main coherence peaks, but not the satellite features due to Leggett modes[33], which are not accounted for in our theory. The resulting fit parameters are listed in Table 1. The best fits for the solutions associated with the E' irreducible representation are obtained by considering strongly selective coupling of the tip to the Γ pockets.

Data availability

All data underpinning the figures has been deposited in the database at https://epub.uni-regensburg.de as item 76,847 under the accession code https://doi.org/10.5283/epub.76847. The full data set for the intermediate steps is too large to be available in a repository, but will be made available upon request to the corresponding author Milena Grifoni (Milena.Grifoni@ur.de).

Code availability

A time-capsule and demonstration of the code used to generate the shown data is available on code ocean under https://doi.org/10.24433/CO.4716423.v1.

References

1. Bardeen, J., Cooper, L. N. & Schrieffer, J. R. Theory of Superconductivity. *Phys. Rev.* **108**, 1175–1204 (1957).
2. Kohn, W. & Luttinger, J. M. New Mechanism for Superconductivity. *Phys. Rev. Lett.* **15**, 524–526 (1965).
3. Friedel, J. XIV. The distribution of electrons round impurities in monovalent metals. *London Edinburgh Philos. Mag. J. Sci.* **43**, 153–189 (1952).
4. Scalapino, D. J. A common thread: The pairing interaction for unconventional superconductors. *Rev. Mod. Phys.* **84**, 1383–1417 (2012).
5. Kallin, C. & Berlinsky, J. Chiral superconductors. *Rep. Prog. Phys.* **79**, 054502 (2016).

6. Hsu, Y.-T., Vaezi, A., Fischer, M. H. & Kim, E.-A. Topological superconductivity in monolayer transition metal dichalcogenides. *Nat. Commun.* **8**, 14985 (2017).
7. Yuan, N. F. Q., Mak, K. F. & Law, K. Possible topological superconducting phases of MoS_2. *Phys. Rev. Lett.* **113**, 097001 (2014).
8. Black-Schaffer, A. M. & Honerkamp, C. Chiral d-wave superconductivity in doped graphene. *J. Phys.: Condens. Matter* **26**, 423201 (2014).
9. Nandkishore, R., Levitov, L. S. & Chubukov, A. V. Chiral superconductivity from repulsive interactions in doped graphene. *Nature Phys* **8**, 158–163 (2012).
10. Scheurer, M. S., Agterberg, D. F. & Schmalian, J. Selection rules for Cooper pairing in two-dimensional interfaces and sheets. *npj Quant Mater* **2**, 1–8 (2017).
11. Ming, F. et al. Evidence for chiral superconductivity on a silicon surface. *Nat. Phys.* **19**, 500–506 (2023).
12. Han, T. et al. Signatures of chiral superconductivity in rhombohedral graphene. *Nature* **643**, 654–661 (2025).
13. Ribak, A. et al. Chiral superconductivity in the alternate stacking compound 4Hb-TaS_2. *Science* **6**, eaax9480 (2020).
14. Silber, I. et al. Two-component nematic superconductivity in 4Hb-TaS_2. *Nat. Commun.* **15**, 824–829 (2024).
15. Wan, Z. et al. Unconventional superconductivity in chiral molecule-TaS_2 hybrid superlattices. *Nature* **632**, 69–74 (2024).
16. Maiti, S. & Chubukov, A. V. Superconductivity from repulsive interaction. *AIP Conf. Proc.* **1550**, 3–73 (2013).
17. Mazin, I. I., Singh, D. J., Johannes, M. D. & Du, M. H. Unconventional superconductivity with a sign reversal in the order parameter of $LaFeAsO_{1-x}F_x$. *Phys. Rev. Lett.* **101**, 057003 (2008).
18. Hirschfeld, P. J., Korshunov, M. M. & Mazin, I. I. Gap symmetry and structure of Fe-based superconductors. *Rep. Prog. Phys.* **74**, 124508 (2011).
19. Hirschfeld, P. J. Using gap symmetry and structure to reveal the pairing mechanism in Fe-based superconductors. *Comptes Rendus Phys.* **17**, 197–231 (2016).
20. Mackenzie, A. P., Scaffidi, T., Hicks, C. W. & Maeno, Y. Even odder after twenty-three years: The superconducting order parameter puzzle of Sr_2RuO_4. *Npj Quantum Mater.* **2**, 1–9 (2017).
21. Cao, Y. et al. Unconventional superconductivity in magic-angle graphene superlattices. *Nature* **556**, 43–50 (2018).
22. Shaffer, D., Kang, J., Burnell, F. J. & Fernandes, R. M. Crystalline nodal topological superconductivity and Bogolyubov Fermi surfaces in monolayer $NbSe_2$. *Phys. Rev. B* **101**, 224503 (2020).
23. Shaffer, D., Burnell, F. J. & Fernandes, R. M. Weak-coupling theory of pair density wave instabilities in transition metal dichalcogenides. *Phys. Rev. B* **107**, 224516 (2023).
24. Hörhold, S., Graf, J., Marganska, M. & Grifoni, M. Two-bands Ising superconductivity from Coulomb interactions in monolayer $NbSe_2$. *2D Mater.* **10**, 025008 (2023).
25. Aase, N. H., Johnsen, C. S. & Sudbø, A. Constrained weak-coupling superconductivity in multiband superconductors. *Phys. Rev. B* **108**, 024509 (2023).
26. Roy, S., Kreisel, A., Andersen, B. M. & Mukherjee, S. Unconventional pairing in Ising superconductors: Application to monolayer $NbSe_2$. *2D Mater.* **12**, 015004 (2024).
27. Akinwande, D. et al. Graphene and two-dimensional materials for silicon technology. *Nature* **573**, 507–518 (2019).
28. Xu, X., Yao, W., Xiao, D. & Heinz, T. F. Spin and pseudospins in layered transition metal dichalcogenides. *Nat. Phys.* **10**, 343–350 (2014).
29. Xi, X. et al. Ising pairing in superconducting $NbSe_2$ atomic layers. *Nat. Phys.* **12**, 139–143 (2016).
30. Zhang, D. & Falson, J. Ising pairing in atomically thin superconductors. *Nanotechnology* **32**, 502003 (2021).
31. Cao, Y. et al. Quality Heterostructures from Two-Dimensional Crystals Unstable in Air by Their Assembly in Inert Atmosphere. *Nano Lett.* **15**, 4914–4921 (2015).
32. Ugeda, M. M. et al. Characterization of collective ground states in single-layer $NbSe_2$. *Nat. Phys.* **12**, 92–97 (2016).
33. Wan, W. et al. Observation of Superconducting Collective Modes from Competing Pairing Instabilities in Single-Layer $NbSe_2$. *Adv. Mat.* **34**, 2206078 (2022).
34. Frigeri, P. A., Agterberg, D. F., Koga, A. & Sigrist, M. Superconductivity without inversion symmetry: MnSi versus $CePt_3Si$. *Phys. Rev. Lett.* **92**, 097001 (2004).
35. Xi, X., Berger, H., Forró, L., Shan, J. & Mak, K. F. Gate tuning of electronic phase transitions in two-dimensional $NbSe_2$. *Phys. Rev. Lett.* **117**, 106801 (2016).
36. Ilić, S., Meyer, J. S. & Houzet, M. Enhancement of the Upper Critical Field in Disordered Transition Metal Dichalcogenide Monolayers. *Phys. Rev. Lett.* **119**, 117001 (2017).
37. Möckli, D. & Khodas, M. Magnetic-field induced *s+if* pairing in Ising superconductors. *Phys. Rev. B* **99**, 180505 (2019).
38. Cho, C.-w et al. Nodal and nematic superconducting phases in $NbSe_2$ monolayers from competing superconducting channels. *Phys. Rev. Lett.* **129**, 087002 (2022).
39. Johannes, M. D., Mazin, I. I. & Howells, C. A. Fermi-surface nesting and the origin of the charge-density wave in $NbSe_2$. *Phys. Rev. B* **73**, 205102 (2006).
40. Xi, X. et al. Strongly enhanced charge-density-wave order in monolayer $NbSe_2$. *Nat. Nanotechnol.* **10**, 765–769 (2015).
41. Hybertsen, M. S. & Louie, S. G. Electron correlation in semiconductors and insulators: Band gaps and quasiparticle energies. *Phys. Rev. B* **34**, 5390–5413 (1986).
42. Rohlfing, M. Electron-hole excitations and optical spectra from first principles. *Phys. Rev. B* **62**, 4927–4944 (2000).
43. Roldán, R., Cappelluti, E. & Guinea, F. Interactions and superconductivity in heavily doped MoS_2. *Phys. Rev. B* **88**, 054515 (2013).
44. Heil, C. et al. Origin of superconductivity and latent charge density wave in NbS_2. *Phys. Rev. Lett.* **119**, 087003 (2017).
45. Sanna, A. et al. Real-space anisotropy of the superconducting gap in the charge-density wave material 2H-$NbSe_2$. *Npj Quantum Mater.* **7**, 6 (2022).
46. Zheng, F. & Feng, J. Electron-phonon coupling and the coexistence of superconductivity and charge-density wave in monolayer $NbSe_2$. *Phys. Rev. B* **99**, 161119 (2019).
47. Das, S., Paudyal, H., Margine, E. R., Agterberg, D. F. & Mazin, I. I. Electron-phonon coupling and spin fluctuations in the Ising superconductor $NbSe_2$. *Npj Comput. Mater.* **9**, 1–9 (2023).
48. Wickramaratne, D., Khmelevskyi, S., Agterberg, D. F. & Mazin, I. Ising superconductivity and magnetism in $NbSe_2$. *Phys. Rev. X* **10**, 041003 (2020).
49. Chubukov, A. V. Kohn-Luttinger effect and the instability of a two-dimensional repulsive Fermi liquid at T=0. *Phys. Rev. B* **48**, 1097–1104 (1993).
50. Liu, G.-B., Shan, W.-Y., Yao, Y., Yao, W. & Xiao, D. Three-band tight-binding model for monolayers of group-VIB transition metal dichalcogenides. *Phys. Rev. B* **88**, 085433 (2013).
51. He, W.-Y. et al. Magnetic field driven nodal topological superconductivity in monolayer transition metal dichalcogenides. *Commun. Phys.* **1**, 40 (2018).
52. Kim, S. & Son, Y.-W. Quasiparticle energy bands and Fermi surfaces of monolayer $NbSe_2$. *Phys. Rev. B* **96**, 155439 (2017).
53. Perali, A. et al. Two-gap model for underdoped cuprate superconductors. *Phys. Rev. B* **62**, R9295–R9298 (2000).
54. Gupta, R. P. & Freeman, A. J. Role of matrix elements in the theoretical determination of generalized susceptibilities in metals. *Phys. Rev. B* **13**, 4376–4386 (1976).

55. Graser, S., Maier, T. A., Hirschfeld, P. J. & Scalapino, D. J. Near-degeneracy of several pairing channels in multiorbital models for the Fe pnictides. *New J. Phys.* **11**, 025016 (2009).
56. Möckli, D. & Khodas, M. Robust parity-mixed superconductivity in disordered monolayer transition metal dichalcogenides. *Phys. Rev. B* **98**, 144518 (2018).
57. Oiwa, R., Yanagi, Y. & Kusunose, H. Theory of superconductivity in hole-doped monolayer MoS_2. *Phys. Rev. B* **98**, 064509 (2018).
58. Oiwa, R., Yanagi, Y. & Kusunose, H. Time-reversal symmetry breaking superconductivity in hole-doped monolayer MoS_2. *J. Phys. Soc. Jpn.* **88**, 063703 (2019).
59. Margalit, G., Berg, E. & Oreg, Y. Theory of multi-orbital topological superconductivity in transition metal dichalcogenides. *Ann. Phys.* **435**, 168561 (2021).
60. Ramezani, H. R. et al. Nonconventional screening of Coulomb interaction in two-dimensional semiconductors and metals: A comprehensive constrained random phase approximation study of mX_2(m=Mo,W,Nb,Ta; x=S,Se,Te). *Phys. Rev. B* **109**, 125108 (2024).
61. Hamill, A. et al. Two-fold symmetric superconductivity in few-layer $NbSe_2$. *Nat. Phys.* **17**, 949–954 (2021).
62. Haniš, J., Milivojević, M. & Gmitra, M. Distinguishing nodal and nonunitary superconductivity in quasiparticle interference of an Ising superconductor with Rashba spin-orbit coupling: The example of $NbSe_2$. *Phys. Rev. B* **110**, 104502 (2024).
63. Tersoff, J. Theory and Application for the Scanning Tunneling Microscope. *Phys. Rev. Lett.* **50**, 1998–2001 (1983).
64. Vaňo, V. et al. Evidence of nodal superconductivity in monolayer 1H-Ta_{S2} with hidden order fluctuations. *Adv. Mat.* **35**, 2305409 (2023).
65. Haim, M., Levchenko, A. & Khodas, M. Mechanisms of in-plane magnetic anisotropy in superconducting $NbSe_2$. *Phys. Rev. B* **105**, 024515 (2022).
66. Nag, P. K. et al. Highly anisotropic superconducting gap near the nematic quantum critical point of $FeSe_{1-x}S_x$. *Nat. Phys.* **21**, 89–96 (2025).
67. Hutchinson, J. & Marsiglio, F. Mixed temperature-dependent order parameters in the extended Hubbard model. *J. Phys.: Condens. Matter* **33**, 065603 (2021).
68. Rubio-Verdú, C. et al. Visualization of Multifractal Superconductivity in a Two-Dimensional Transition Metal Dichalcogenide in the Weak-Disorder Regime. *Nano Lett.* **20**, 5111–5118 (2020).
69. Horcas, I. et al. WSXM: A software for scanning probe microscopy and a tool for nanotechnology. *Rev. Sci. Instrum.* **78**, 013705 (2007).
70. Inosov, D. S. et al. Crossover from weak to strong pairing in unconventional superconductors. *Phys. Rev. B* **83**, 214520 (2011).

Acknowledgements

Funding was provided by the project B09 of CRC 1277 of the Deutsche-Forschungsgemeinschaft, J.Si., the RTG 2905 - 502572516 of the Deutsche-Forschungsgemeinschaft, A.B., the grant no. G83-27 from the Interdisciplinary Centre for Mathematical and Computational Modelling (ICM) of the University of Warsaw (UW), and the V4-Japan project BGapEng V4-JAPAN/2/46/BGapEng/2022 by the National Center for Research and Development (NCBR), M.K., the ERC Starting grant LINKSPM (Grant #758558) and the grant PID2023-153277NB-I00 funded by the Spanish Ministry of Science, Innovation and Universities, M.M.U. M.K. appreciates discussions with Timon Moško. M.M. appreciates helpful discussions with Fernando de Juan, Martin Gmitra and Cosimo Gorini, and acknowledges thankfully the help of Andrea Donarini and Marko Milivojevic in constructing the basis functions. J.Si. appreciates discussions with Rui Shi and acknowledges his help by pointing out a mistake in a previous version of this manuscript.

Author contributions

J.Si. and M.M. performed the analytical and numerical tight-binding calculations. M.K. calculated the DFT band structure and polarisability. W.W. and M.M.U. performed the STM/STS experiments on the monolayer $NbSe_2$. A.B. and J.Si. performed the fitting to the experimental data. M.G. conceived the project, leading with M.M. the theoretical analysis with support from J.Si. and J.Sc.; M.M.U. was responsible for the experimental part of this work. The manuscript was written by M.G., J.Si. and M.M. with contributions from all other authors.

Competing interests

The authors declare no competing interests.

Additional information

Supplementary information The online version contains supplementary material available at https://doi.org/10.1038/s41467-025-63319-z.

Correspondence and requests for materials should be addressed to Julian Siegl or Milena Grifoni.

Peer review information *Nature Communications* thanks Daniel Shaffer, and the other, anonymous, reviewer(s) for their contribution to the peer review of this work. A peer review file is available.

Reprints and permissions information is available at http://www.nature.com/reprints